


RESEARCH

Open Access



# Efficient delivery of anlotinib and radioiodine by long circulating nano-capsules for active enhanced suppression of anaplastic thyroid carcinoma

Linlin Zhang<sup>1†</sup>, Chuanying Zhu<sup>2†</sup>, Shuo Huang<sup>1†</sup>, Miaomiao Xu<sup>1,3†</sup>, Chao Li<sup>1</sup>, Hongliang Fu<sup>1</sup>, Yafu Yin<sup>1</sup>, Sheng Liang<sup>1\*</sup>, Hui Wang<sup>1\*</sup>, Zhilei Cui<sup>4\*</sup> and Lei Huang<sup>5,6\*</sup> 

## Abstract

<sup>131</sup>I therapy is clinically unfeasible for anaplastic thyroid carcinoma (ATC), due to lack of active targets and ATC's resistance to radiation. Novel radionuclide-labeled targeted nano-drug delivery systems have exhibited the potential of prominent tumor imaging and remedy. Capitalizing on recent research achievements in nanotechnology and nuclear medicine, we sought to develop a radiolabeled nano-drug, which could specifically accumulate in ATCs via tumor-selective targeted delivery system and which could treat the tumors with both targeted and radionuclide therapeutics. Epidermal growth factor receptor (EGFR) and mutant P53 expressions were positive in 80% and 60% of patients with ATC, respectively. Herein, core-shell nanoparticles-based poly (ethyleneglycol)-crosslinker (PEG-CL) was fabricated, by encapsulating bovine serum albumin (BSA) inside the core and an enzyme with various tyrosine residues for <sup>131</sup>I radiolabeling, and by loading anlotinib, a multi-kinase inhibitor which can site-selectively target overexpressed EGFR in ATC cells and which also suppresses angiogenesis, onto the PEG-CL shell surface. The Anlotinib-BSA nano-capsule (nBSA) showed a mostly uniform size distribution centering at 21–23 nm, and the nano-drug had a characteristic absorption peak at the wavelength of 325 nm. The Anlotinib-nBSA had a high labeling efficiency with the radiochemical purity being approximately 100%. The cellular uptake efficiency of Anlotinib-nBSA-<sup>131</sup>I was much higher than that of free <sup>131</sup>I in both 8305C (3.6% vs 0.0%) and C643 (7.0% vs 0.1%; with a higher EGFR expression level) ATC cell lines. Anlotinib-nBSA-<sup>131</sup>I showed the strongest cytotoxicity against ATC cells with different concentrations of anlotinib, and induced the highest rate of apoptosis (C643 cells, 81.7%). The nanoparticles could actively target tumor surface with anlotinib exhibiting enhanced radio-sensitization effects by functionally upregulating P53 and Bax. In vivo SPECT/CT imaging showed that the concentration of Anlotinib-nBSA-<sup>125</sup>I in tumors peaked

<sup>†</sup>Linlin Zhang, Chuanying Zhu, Shuo Huang, and Miaomiao Xu have contributed equally to this work.

\*Correspondence:

Sheng Liang

liangsheng364214@163.com

Hui Wang

Wanghui@xinhuamed.com.cn; huiwangshanghai@163.com

Zhilei Cui

cuizhilei@xinhuamed.com.cn

Lei Huang

lei.huang@alumni.dkfz.de; huangleizhenting@126.com

Full list of author information is available at the end of the article

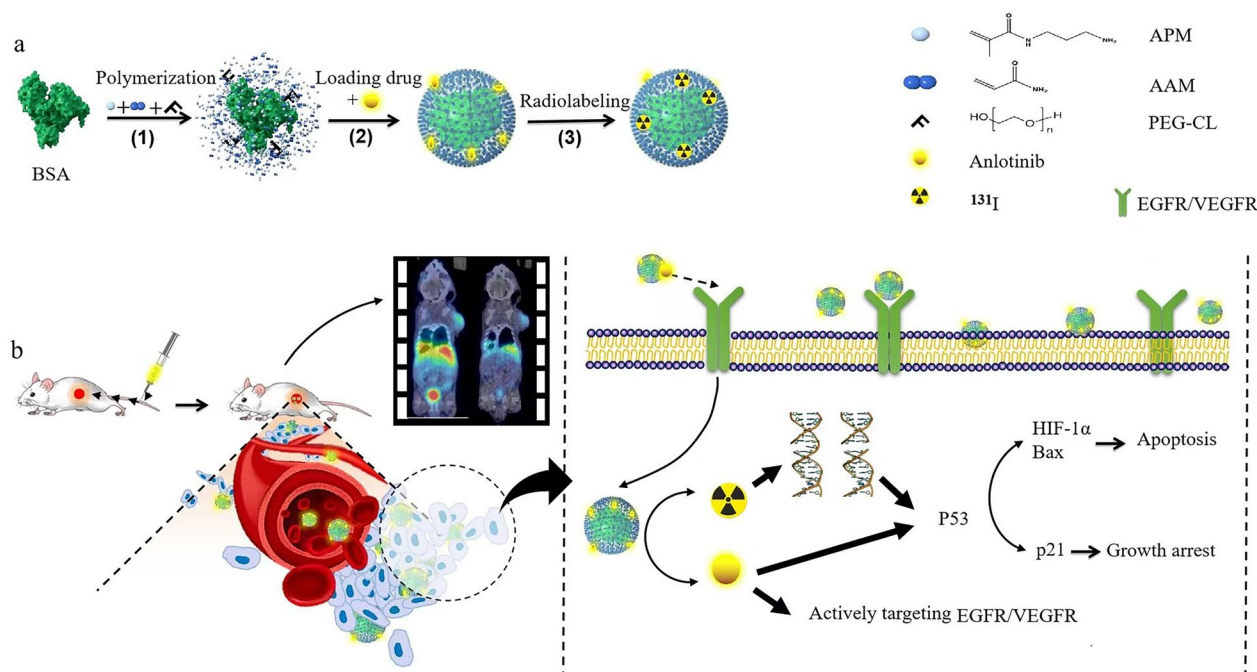


© The Author(s) 2025. **Open Access** This article is licensed under a Creative Commons Attribution-NonCommercial-NoDerivatives 4.0 International License, which permits any non-commercial use, sharing, distribution and reproduction in any medium or format, as long as you give appropriate credit to the original author(s) and the source, provide a link to the Creative Commons licence, and indicate if you modified the licensed material. You do not have permission under this licence to share adapted material derived from this article or parts of it. The images or other third party material in this article are included in the article's Creative Commons licence, unless indicated otherwise in a credit line to the material. If material is not included in the article's Creative Commons licence and your intended use is not permitted by statutory regulation or exceeds the permitted use, you will need to obtain permission directly from the copyright holder. To view a copy of this licence, visit <http://creativecommons.org/licenses/by-nc-nd/4.0/>.

at 24 h, and the intense signal persisted for at least one week. Anlotinib-nBSA-<sup>131</sup>I showed the strongest tumor inhibition effects in tumor-bearing mice, with no evident pathological changes observed. Together, the optimal nanoparticles co-loading anlotinib and <sup>131</sup>I satisfactorily demonstrated efficient drug delivery and prominent antitumor effects both in vitro and in vivo, without obvious in vivo bio-toxicity. Our innovation could offer novel effective strategies for targeted management of ATC, a highly-aggressive disease with dismal prognosis.

**Keywords** Anlotinib- and <sup>131</sup>I-delivering nanoparticles, Anaplastic thyroid carcinoma (ATC), Targeted nano-drug delivery, Efficacy, Safety

## Graphical Abstract



## Introduction

Thyroid cancer (TC) is the most common malignancy among endocrine and head-and-neck cancers, accounting for more than 586,000 new cancer cases and approximately 44,000 cancer-related deaths worldwide in 2020. Anaplastic thyroid carcinoma (ATC) is the most aggressive histopathology type of TCs, and often metastasizes very early, leaving no room for resection [1]. While accounting for only 1% to 2% of total TC cases, ATCs are linked to half of TC-related fatalities, partly because of resistance to radiation with difficulties in concentrative uptake of the radioiodine iodine-131 (<sup>131</sup>I) [2]. Also, no effective chemotherapy regimens exist for ATC.

Significant challenges have emerged when attempting to alter the low treatment response rate for ATC. Numerous efforts have been made to tackle this tough problem for decades, albeit with limited progress. To date, two

major approaches have been explored. The first approach relies on gene transfection technique to introduce *NIS* and *TPO* genes into ATC lesions to recover iodine uptake capacity [3]. However, after the transfection, rapid outflow of reuptake iodine results in too short residence time of <sup>131</sup>I, making it too difficult to kill the cancer cells. The second method enables elevated iodine reuptake ability of some cells through the usage of drugs which can regulate cell proliferation and differentiation (e.g., retinoic acid and rosiglitazone), but it still has limitations, including severe side effects and the inability to solve the problem of steady rise of iodine in TC cells. Thus, innovative and effective treatment is strongly and urgently needed for ATC.

Over the last few decades, significant advances have been achieved in the understanding of the molecular pathogenesis of TC, and molecular targeted therapy is

a promising treatment approach for ATC, which barely has other alternative treatment [1, 4]. Recently, there has been a convergence of evidence suggesting that non-small cell lung cancers (NSCLCs) harboring *TP53* mutation are more likely to respond to VEGF/VEGFR inhibitors, such as anlotinib and sorafenib [5, 6]. Cancer cells harboring *TP53* mutation frequently exhibit insensitivity to radiation[7]. *TP53* is one of the most frequently-mutated genes in ATC [1, 8–10]. Acting on the mutant *TP53* gene may be a key to the treatment sensitivity for ATC.

Anlotinib is a novel, orally-administered receptor tyrosine kinase inhibitor (TKI) that targets vascular endothelial growth factor receptor (VEGFR)-1, VEGFR-2, VEGFR-3, epidermal growth factor receptors (EGFRs), fibroblast growth factor receptors (FGFRs), platelet-derived growth factor receptors (PDGFR), and c-KIT, and suppresses the activity of these oncoproteins. It demonstrates promising efficacy against a wide variety of tumors in preclinical models, including advanced/metastatic NSCLC and ATC [11]. P53 with loss of function due to *TP53* mutation in TC cells with deficiency in transactivation function can be reactivated by anlotinib [12]. Anlotinib has the potential to treat advanced/metastatic TC; nevertheless, most studies have only examined

anlotinib monotherapy [13]. Notably, the overall incidence of any adverse events (AEs) associated with anlotinib is nearly 100%, and 29% of patients report Grade 3–4 AEs, including hand-foot-skin reaction (5%), hypertension (10%), triglyceride elevation (10%), and lipase elevation (5%)[14]. Hence, it is urgently required to develop an advanced combination strategy of anlotinib with other therapeutics.

Accumulating evidence has suggested that nanocarrier drugs with specific targeting capacity could be nontoxic and/or biodegradable with controllable release [15, 16]. Wang et al. [17] reported that both active targeting and effectively-reduced VEGF levels were observed with the multifunctional IR825@Bev-PLGA-PFP Nanoparticles (NPs) platform. Our group has previously shown that a CD44-targeting delivery system with the self-assembled hyaluronic acid (HA)–polyethyleneimine (PEI) nanoparticle, which could be labeled by <sup>131</sup>I and loaded with a mutant-P53-restoring regent, Prima-1, could provide potential direction for ATC theranostics [18]. Our previous work has provided a platform with capability for the delivery of protein drugs with improved therapeutic efficacy, prolonged circulation time, and reduced immunogenicity. Based on this and considering that the conventional oral <sup>131</sup>I treatment cannot work for ATC, herein we further developed a novel delivery approach

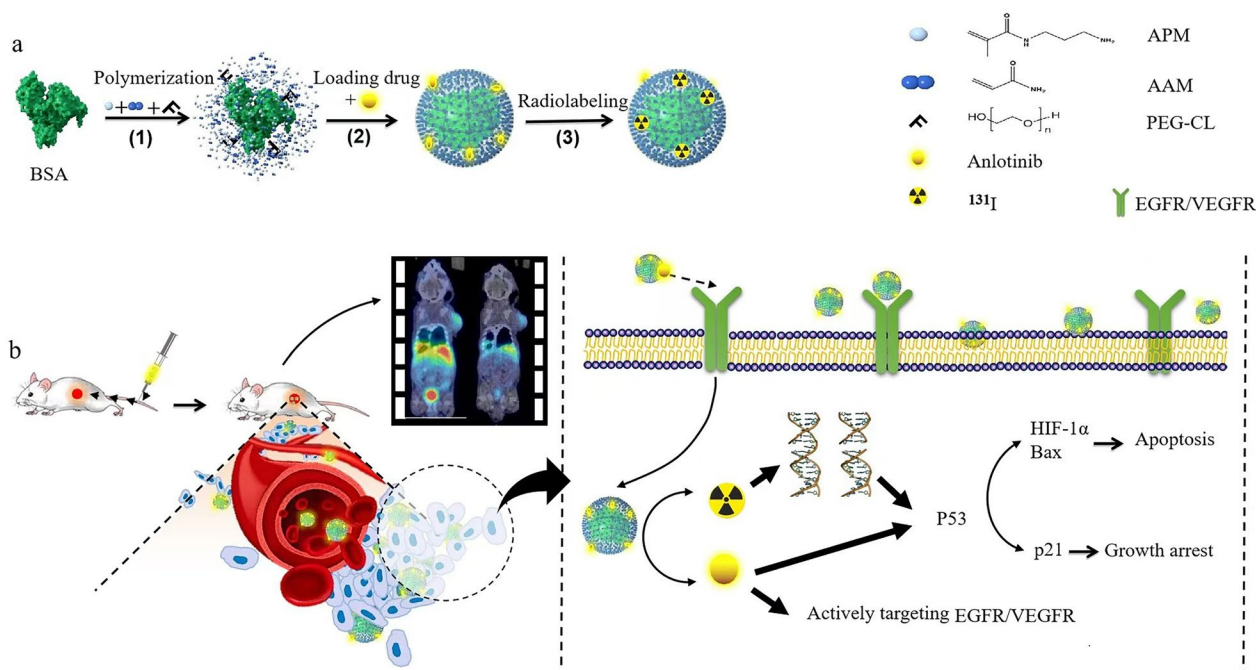


**Fig. 1** Schematic illustration of the preparation and synthesis of radiolabeled <sup>131</sup>I-anlotinib-nBSA nanoparticles. **a** Conjugate synthesis, PEGylation assembly, drug loading, and radioactive iodine labeling; **b** molecular mechanisms of radionuclide therapy sensitization by anlotinib. BSA, bovine serum albumin; nBSA, nano-capsules of bovine serum albumin; EGFR, epidermal growth factor receptor; VEGFR, vascular endothelial growth factor receptor

that enables an active, efficient, and targeted entry of  $^{131}\text{I}$ -radionuclide accompanied with anlotinib into the tumor site. We examined the assumption that anlotinib and  $^{131}\text{I}$  based on the nanoplatform could have enhanced effects on ATC, and mechanistically explored the potential underlying signaling pathway.

In this study, we constructed a novel agent, using nanocarriers with qualified features of active targeting, which were loaded with anlotinib and radiolabeled with  $^{131}\text{I}$ , with longer retention time in tumor tissue (Fig. 1). We used nanoparticles to parcel the  $^{131}\text{I}$ -iodinated tyrosine residues. In order to improve the *in vivo* targeting property of radioactive iodine on bovine serum albumin (BSA) nano-capsule, we carefully modified the nanoparticle surface. Herein we demonstrated a general design of a robust BSA nanocomplex delivery system with radionuclide-labeling, which would make the nanocarriers remain longer in plasma, thus providing more opportunities for the carriers to target tumor. BSA was assembled or conjugated to form a stable nanoparticle core, which has various residues for radiolabeling (e.g., tyrosine and amide) [19]. Subsequently,

the core was encapsulated within a crosslinked polymer nano-capsule, and the nanoparticle surface was modified with the TKI anlotinib, which not only possesses active targeting capacity but also can inhibit both tumor angiogenesis and tumor cell proliferation and induce apoptosis [20]. The multi-kinase inhibitor anlotinib can directly target and block VEGFR and EGFR whose positive expression rates are high in ATC [21–25], and has shown promising anti-ATC effects with good safety [12, 26]. Partly due to high affinity to VEGFR and EGFR, the anlotinib-based core-shell nanocarriers, including cationic polymers, nanogels, and crosslinking nanoparticles, exhibited impressive site-selective targeting function. The targeted drug anlotinib possesses both active targeting and therapeutic functions, and the Anlotinib-nBSA nanocarrier can be precisely delivered to the ATC cell also with enhanced permeability and retention (EPR) effect [18, 27–32] facilitating enrichment in ATC; simultaneously, the core-shell nanoparticle can site-selectively carry  $^{131}\text{I}$  to the tumor cell for radionuclide therapy which causes DNA damage and double-strand breaks (DSBs) and induces apoptosis in

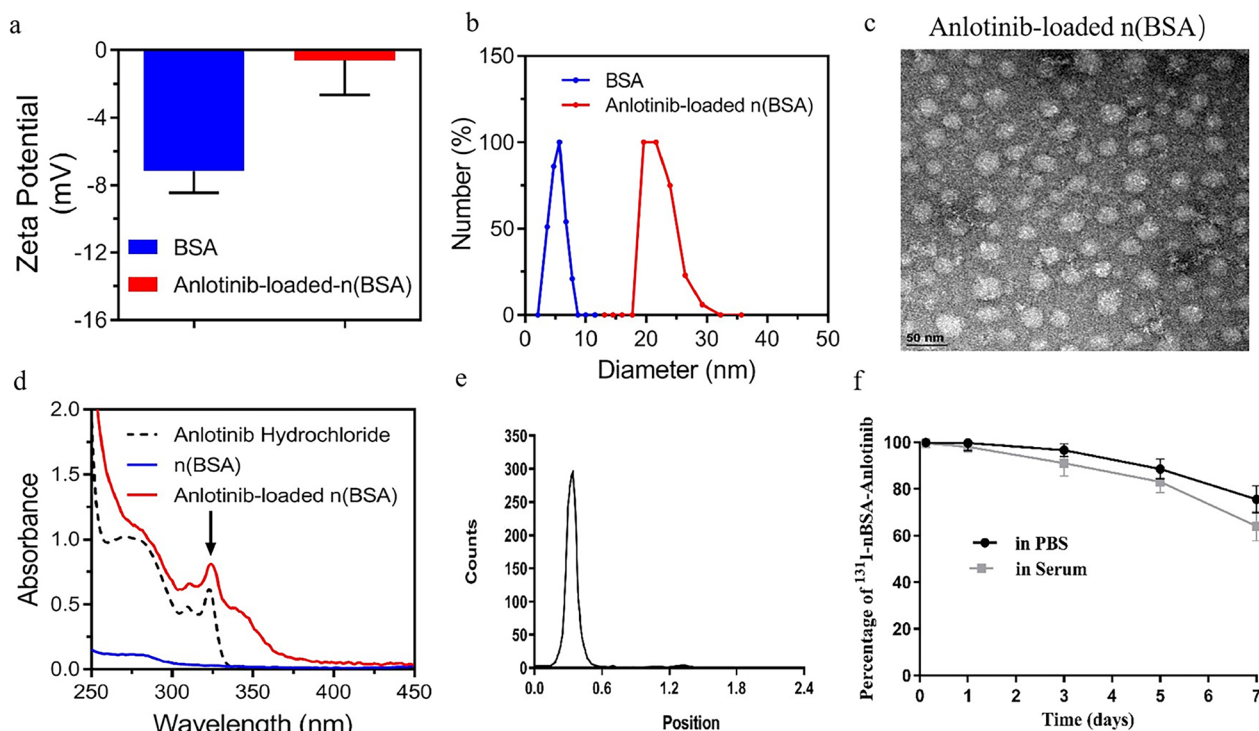


**Fig. 2** Characteristics of Anlotinib-nBSA. **a** Zeta potentials and **b** particle size distributions of native BSA and Anlotinib-nBSA. **c** Representative transmission electron microscopic (TEM) image of Anlotinib-nBSA showing the formation of nano-capsules with spherical morphology. **d** The drug had a characteristic absorption peak at the wavelength of 325 nm, indicating that the drug had been successfully loaded onto the nano-capsules. **e** The radiochemical impurity of Anlotinib-nBSA- $^{131}\text{I}$ . The radioiodine-labeling rate of Anlotinib-nBSA- $^{131}\text{I}$  was determined by thin-layer chromatography (TLC) with  $\text{ddH}_2\text{O}$  as the separation agent, and the result showed the radioiodine-labeling rate was nearly 100%. **f** The stability of radioiodine-labeled Anlotinib-nBSA- $^{131}\text{I}$  in phosphate buffered saline (PBS) buffer (1 mM; pH = 7.4) or serum at 37 °C, measured by relative scattering light intensity. Data are presented as mean  $\pm$  standard error from 3 independent experiments

ATC [33, 34]. Anlotinib also exhibited significant radiosensitization effects through the functional upregulation of P53 in ATC [12, 18, 35]. The anlotinib and <sup>131</sup>I combination treatment based on such targeting nano-systems exhibited significantly-effective therapeutic effects against ATC in mouse models, with markedly-reduced toxicity.

**Results**

**Positive expression rates of EGFR and mutant P53 were high in tumor samples of patients with ATC**

We first employed immunohistochemistry and investigated the levels of EGFR and mutant P53 expressions in

tumor tissues from 15 patients with ATC, whose resected specimen is hard to obtain due to its low incidence and usually advanced unresectable stage at diagnosis. We observed positive expression of EGFR, a potential treatment target in ATC, in 12 out of 15 patients with ATC (80%). Mutant P53 expression was positive in 9 out of 15 patients (60%) (Figure S1a-b).

**Synthesis and characterization of Anlotinib-nBSA-<sup>131</sup>I nanoparticles**

The nano-capsules of BSA (nBSA), where BSAs were encapsulated within thin network-polymer shells by in situ polymerization, is illustrated in Fig. 1. Figure 2

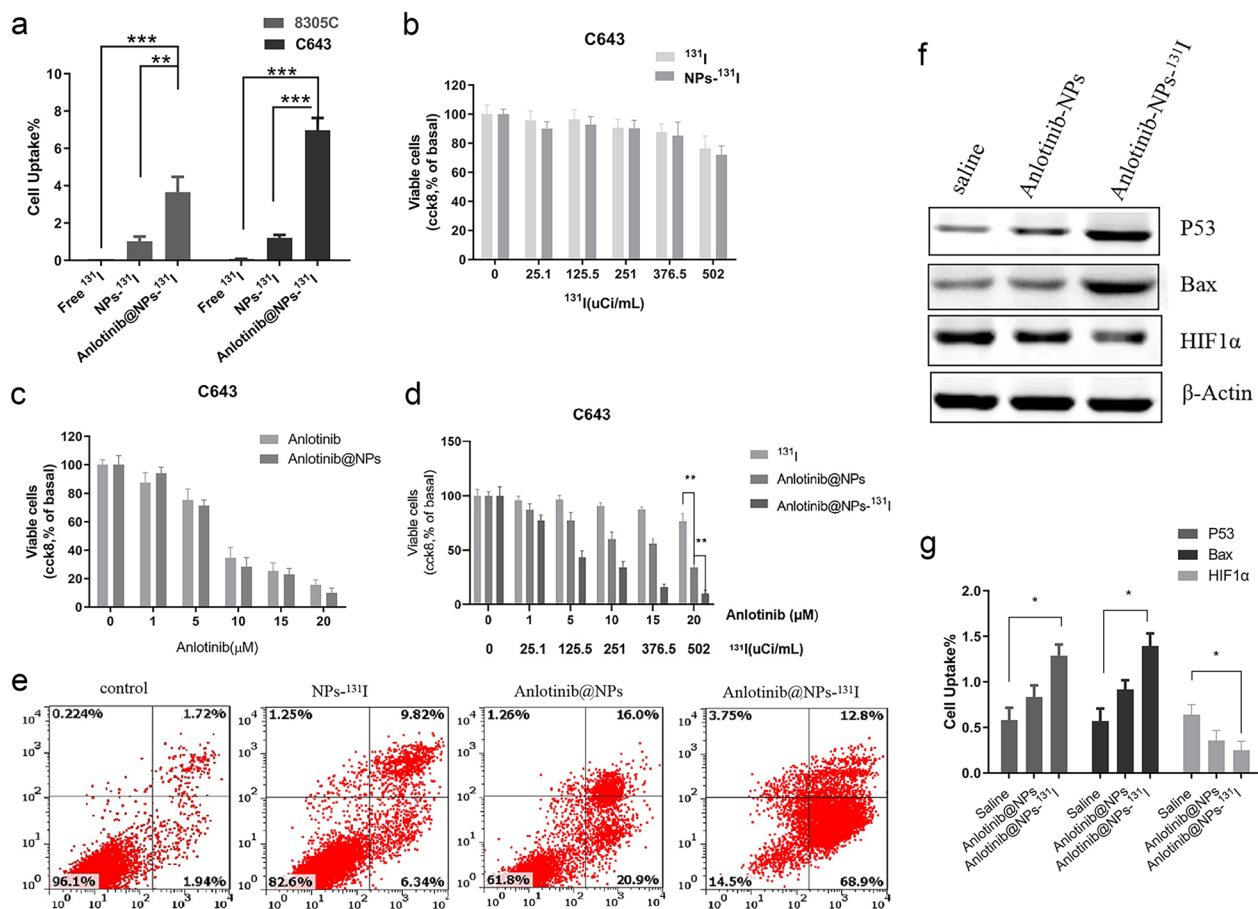


**Fig. 3** Properties of nano-capsule in vitro. **a** The cellular uptake of free <sup>131</sup>I, <sup>131</sup>I-nBSA (<sup>131</sup>I-NPs), and Anlotinib-nBSA-<sup>131</sup>I (Anlotinib@NPs-<sup>131</sup>I) was measured by gamma-counter after 1-h incubation of 8305C and C643 cells. **b** The relative viability of C643 cells after being treated with various concentrations of <sup>131</sup>I or <sup>131</sup>I-nBSA for 48 h. **c** The relative viability of C643 cells after being treated with various concentrations of anlotinib or Anlotinib-nBSA (Anlotinib@NPs) for 48 h. **d** The relative viability of C643 cells after being treated with various concentrations of <sup>131</sup>I, Anlotinib-nBSA, or Anlotinib-nBSA-<sup>131</sup>I for 48 h (n = 5 per group; \*P < 0.05, \*\*P < 0.01, \*\*\*P < 0.001). **e** Cell apoptosis was detected after cells being treated with control saline, <sup>131</sup>I-NPs, Anlotinib@NPs, or Anlotinib@NPs-<sup>131</sup>I for 48 h by a FITC – annexin V/PI flow cytometry assay. Dots in the upper left and right correspond to cells in the necrotic and late apoptotic states, respectively, while dots in the lower left and right represent the living and early apoptotic cells, respectively. **f** P53, Bax, and HIF-1α were detected using Western blot with treatment by saline, Anlotinib@NPs, or Anlotinib@NPs-<sup>131</sup>I for 24 h (we chose 116.5 μCi/mL <sup>131</sup>I, corresponding to 10 mM anlotinib). **g** Relative quantities of P53, Bax, and HIF-1α were detected after treatment with saline, Anlotinib@NPs, or Anlotinib@NPs-<sup>131</sup>I. (\*P < 0.05, \*\*P < 0.01, \*\*\*P < 0.001). nBSA, nano-capsules of bovine serum albumin; NPs, nanoparticles

shows the zeta potential and size distribution of native BSA and Anlotinib-nBSA, respectively, obtained by zDLS. The native BSA exhibited negative charge ( $\approx -7$  mV) with a size distribution centering at 5–7 nm. Comparatively, Anlotinib-nBSA showed nearly neutral charge ( $\approx 0$  mV) and a size distribution centering at 21–23 nm (Fig. 2a, b).

The chemical structure of the Anlotinib-nBSA nanoparticle was assessed by  $^1\text{H-NMR}$  using  $\text{D}_2\text{O}$  as the solvent (Figure S2a). Anlotinib stock solution was added into nBSA solution with a molar ratio of 150:1, and the standard curve for determination of drug content is shown in Figure S2b. As illustrated in a representative transmission electron microscopic (TEM) image (Fig. 2c), Anlotinib-nBSA exhibited uniform distribution, which was consistent with the DLS measurement. UV–visible spectrophotometer manifested that the drug had a characteristic absorption peak at the wavelength of 325 nm (Fig. 2d). After Anlotinib-nBSA was assembled, it was radio-iodinated by the Iodogen method. Radioactive thin-layer chromatography (TLC) further demonstrated high labeling efficiency of Anlotinib-nBSA (Fig. 2e) with the radiochemical purity being approximately 100%. Furthermore, Anlotinib-nBSA- $^{131}\text{I}$  was incubated in PBS or serum at 37 °C for evaluation of radiolabeling stability. Anlotinib-nBSA- $^{131}\text{I}$  nanoparticles exhibited high radiolabeling stability in PBS and serum after incubation for 7 days, and it was slightly more stable in phosphate buffered saline (PBS) than in serum at all of the timepoints (Figs. 2f and S2).

### In vitro cellular uptake

To evaluate  $^{131}\text{I}$  delivery efficiency of the nano-capsule into ATC cells, the cellular uptake of Anlotinib-nBSA- $^{131}\text{I}$  and free  $^{131}\text{I}$  was calculated by a gamma-counter in both 8305C and C643 cell lines. We also investigated the relative viabilities of the two cell lines after being treated with various concentrations of anlotinib for 48 h (Figure S3). The cellular uptake of Anlotinib-nBSA- $^{131}\text{I}$  was much higher than that of free  $^{131}\text{I}$  in both 8305C and C643 cell lines, and interestingly, C643 cells with a higher EGFR expression level had a higher uptake efficiency than 8305C cells (Fig. 3a). We chose C643 cells as our subsequent target cell.

### In vitro cytotoxicity and apoptosis-inducing assays

In order to investigate whether anlotinib, a promising active targeted small-molecule drug, was able to restore the radiosensitivity of ATC cells, cytotoxicity test was performed. First, we verified the safety of the material through testing the relative viabilities of C643 cells after being treated with various concentrations of nBSA nanoparticle for 48 h (Figure S4).

Also, we compared the cytotoxicity between free  $^{131}\text{I}$  and nBSA- $^{131}\text{I}$  in C643 cells. nBSA- $^{131}\text{I}$  displayed a little stronger cytotoxicity than free  $^{131}\text{I}$  under the same radioactivity (Fig. 3b). The data showed similar outcomes between the Anlotinib-nBSA and free anlotinib groups at different concentrations (Fig. 3c). Subsequently, the cytotoxicity of free  $^{131}\text{I}$ , Anlotinib-nBSA nanoparticles (NPs), and Anlotinib-nBSA- $^{131}\text{I}$  NPs was evaluated in C643 cells by CCK-8 assay. Anlotinib-nBSA NPs and Anlotinib-nBSA- $^{131}\text{I}$  NPs showed obvious cytotoxicity

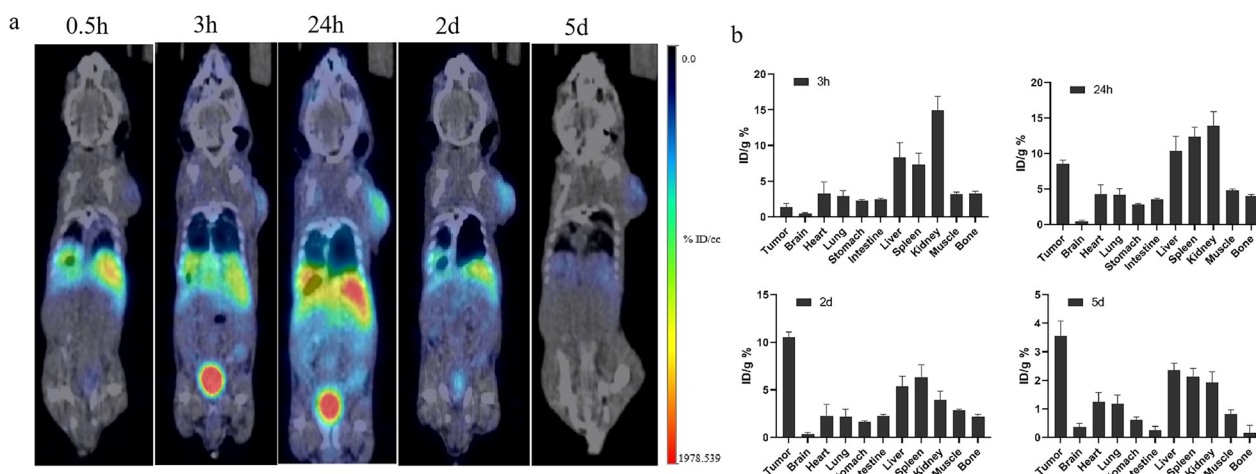


**Fig. 4** In vivo SPECT/CT imaging and biodistribution. **a** SPECT/CT imaging of nude mice with subcutaneous C643 tumor implant after intravenous injection of  $^{125}\text{I}$ -Anlotinib-nBSA at various post-injection timepoints. **b** Biodistribution of  $^{125}\text{I}$ -Anlotinib-nBSA in various organs measured by the gamma-counter at 3 h, 24 h, 2 days, and 5 days after injection ( $n=5$ )

in C643 cells with different concentrations of anlotinib (1, 5, 10, 15, and 20 mM) after co-incubation for 48 h (Fig. 3d). Compared with the other two groups, the Anlotinib-nBSA-<sup>131</sup>I NP group showed the best tumor-inhibition ability.

Then we performed apoptosis assay using flow cytometry to investigate whether the cytotoxicity of <sup>131</sup>I and anlotinib were associated with apoptosis. <sup>131</sup>I-Anlotinib-nBSA induced a significantly higher rate of apoptosis in C643 cells than the other three groups (control, <sup>131</sup>I-nBSA, and Anlotinib-nBSA), which was in accordance with the CCK-8 assay findings (Fig. 3e). Findings were similar in 8305C cells (Figure S5).

**Molecular mechanisms of radiotherapy sensitization by anlotinib**

To further investigate the mechanism underlying how anlotinib sensitized <sup>131</sup>I radiotherapy in ATC cells, the expression levels of apoptosis-related proteins, including P53 and its downstream molecules (Bax and HIF-1α), were detected by Western blot after treatment with <sup>131</sup>I-nBSA, Anlotinib-nBSA, or <sup>131</sup>I-Anlotinib-nBSA in C643 cells. Compared with the control

cells incubated with <sup>131</sup>I-nBSA, the levels of P53 and Bax in the <sup>131</sup>I-Anlotinib-nBSA group were significantly increased. Also, incubation with Anlotinib-nBSA showed slightly-increased P53 and Bax. (Fig. 3f, g).

**In vivo SPECT/CT imaging and biodistribution**

We chose <sup>125</sup>I as a more appropriate radionuclide for SPECT/CT imaging due to the low-energy γ-ray and long half-life (60 days). In vivo micro-SPECT imaging confirmed the tumor location and volume at the left flank of the mice subcutaneously bearing tumor grafts; meanwhile free <sup>125</sup>I rarely accumulated at tumor sites and was mostly excreted through biliary tract and/or bladder within 24 h. <sup>125</sup>I-Anlotinib-nBSA was concentrated especially in major organs, such as liver, spleen, kidney, and bladder, 30 min after the intravenous injection, and only weak radioactivity was detected in the tumor sites. Subsequently, the uptake amount of the aforementioned organs descended following blood circulation, while the concentration in tumors increased gradually and approached the peak level at 24 h. SPECT/CT imaging showed an intense and persistent signal of tumor sites in all time during the one-week period of observation. There seemed to be

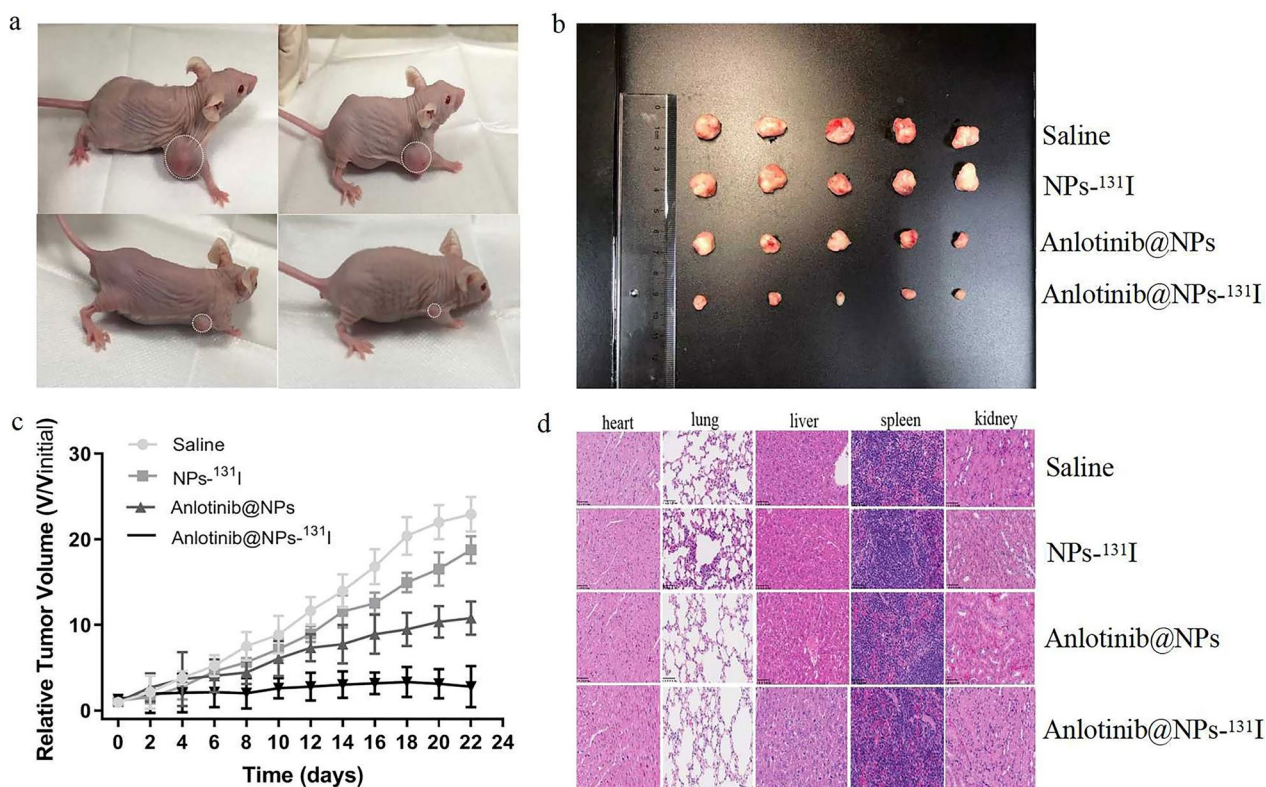


**Fig. 5** In vivo antitumor activity and biosafety evaluations. **a** and **b** The images of C643 tumors with different treatment. **c** Relative tumor growth curves in different treatment groups (n = 5 per group). **d** H&E-stained images of heart, lung, liver, spleen, and kidney from mice in different treatment groups

some radioactive signals from the tail vein injection site even after 24 h post intravenous injection, which might indicate the nanoparticles accumulation on the injection site possibly due to the punctured vein. (Fig. 4a).

To further quantitatively analyze the biodistribution of  $^{125}\text{I}$ -Anlotinib-nBSA, the radioactivity in various organs and tumor tissues was measured by the gamma-counter.  $^{125}\text{I}$ -Anlotinib-nBSA displayed a high uptake in tumor site, where the radioactivity nearly approached the liver uptake at 24 h. At 3 h, 4 h, and 2 days after intravenous injection, there was an accumulation of nanoparticles in the intestine; the accumulation level was relatively low ( $<4$  ID/g %) and decreased to 1 ID/g % on day 5. The accumulation in the intestine might be possibly explained by that during systemic biodistribution after intravenous injection, a small proportion of the nanoparticles also entered the intestine which is rich in blood vessels and remained there for a certain period, and that there might also be a certain level of VEGFR and/or EGFR expression in the intestine. The intestine accumulation of nanoparticles is also reported in previous studies [34, 36] (Fig. 4b).

#### **In vivo antitumor activity and biosafety evaluations**

In order to investigate the enhanced effect of Anlotinib-nBSA- $^{131}\text{I}$  in vivo, the growth of C643 tumors was evaluated after intravenous injection of saline,  $^{131}\text{I}$ -nBSA (200  $\mu\text{Ci}$  of  $^{131}\text{I}$ ), Anlotinib-nBSA (100  $\mu\text{g}$  of anlotinib), or Anlotinib-nBSA- $^{131}\text{I}$  (200  $\mu\text{Ci}$  of  $^{131}\text{I}$ , corresponding to 100  $\mu\text{g}$  of anlotinib). Through dynamically measuring tumor growth, the three treatment groups displayed obvious antitumor effects compared with the control group (Fig. 5a, b). Furthermore, Anlotinib-nBSA- $^{131}\text{I}$  treatment significantly delayed tumor growth in comparison with the  $^{131}\text{I}$ -nBSA and Anlotinib-nBSA groups (Fig. 5c). The body weight of mice showed the same trend as tumor weight (Figure S6).

To determine whether the targeted delivery systems could be translated into clinical application, we also performed the biosafety test. The toxicity of the saline,  $^{131}\text{I}$ -nBSA, Anlotinib-nBSA, and Anlotinib-nBSA- $^{131}\text{I}$  groups were evaluated systematically by hematoxylin and eosin (H&E) staining, liver function test, and kidney function test. No evident pathological changes were observed in the treatment groups in comparison with the control groups (Fig. 5d).

#### **Discussion**

$^{131}\text{I}$  therapy is clinically unfeasible for ATC, due to lack of active targets and ATC's resistance to radiation. Novel radionuclide-labeled targeted nano-drug delivery systems have exhibited the great potential of prominent tumor imaging and remedy. There have been exciting and important breakthroughs in nanomedicine for cancer

theranostics. The successfully designed bioresponsive carbon nano-gated multifunctional mesoporous silica can greatly assist with noninvasive targeted drug delivery and bioimaging for effective cancer treatment and diagnosis [37]. Plasmonic carbon nanohybrids (gold deposited plasmonic polylactic-co-glycolic acid nanoshells decorated graphene oxide nanosheets, GO-AuPLGA) have the great potential for repetitive and highly localized photothermal cancer ablation therapy, without causing side effects on neighboring healthy cells [38]. Ultrahigh penetration and retention of graphene quantum dot mesoporous silica nanohybrids has greatly contributed to image guided tumor regression [39]. The plasmonic supramolecular organic-inorganic nanohybrid can serve as a contrast agent for site-selective imaging and detection of cancer [40].

Capitalizing on recent research achievements in nanotechnology and nuclear medicine, herein we developed a radiolabeled nano-drug, Anlotinib-nBSA- $^{131}\text{I}$ , which could specifically accumulate in ATCs via tumor-selective targeted delivery system and which could treat the tumors with both targeted and radionuclide therapeutics. Core-shell nanoparticles-based poly (ethyleneglycol)-crosslinker (PEG-CL) was fabricated, by encapsulating BSA inside the core and an enzyme with various tyrosine residues for  $^{131}\text{I}$  radiolabeling, and by loading anlotinib, a multi-kinase inhibitor which can target overexpressed VEGFR and EGFR in ATC, onto the PEG-CL shell surface. The optimal  $^{131}\text{I}$ -labeled nanoparticles satisfactorily demonstrated efficient  $^{131}\text{I}$  delivery and prominent antitumor effects both in vitro and in vivo, without obvious in vivo bio-toxicity. Based on the active tumor-targeting property of anlotinib [21–25] and the enhanced permeability and retention (EPR) effect [18, 27–32] of the nanocarrier, the newly developed nano-drug could be precisely delivered to the ATC site, where the anlotinib component suppresses tumor cell proliferation and angiogenesis and the  $^{131}\text{I}$  component simultaneously exerts its radionuclide therapy function. Also, anlotinib in the nanoparticles exhibited significant radio-sensitization effects through functionally upregulating P53 in ATC [12, 18, 35]. This innovation could offer novel effective strategies for the targeted management of ATC, a highly-aggressive and treatment-resistant malignancy with dismal prognosis and with very limited treatment options, potentially improving outcomes for patients with this challenging disease.

Anlotinib-nBSA showed nearly neutral charge and a size distribution centering at 21–23 nm, suggesting the successful formation of the polymer on the BSA protein. Successful encapsulation was also observed by UV-visible spectrophotometer, which indicated that the drug had been loaded onto the nano-capsules. Despite the



lack or absence of a surface charge, the Anlotinib-nBSA nano-formulation can exhibit notable stability in serum or body fluids. While surface charge is an important factor for stability of nanoparticles, there are also other factors importantly impacting the stability. The nano-formulation Anlotinib-nBSA was synthesized using poly (ethylene glycol)-crosslinker (PEG-CL) as a crosslinker reagent. Poly (ethylene glycol) (PEG) is a neutral and hydrophilic polymer that achieves hydration via hydrogen bonding, providing a unique surface that resists nonspecific protein adsorption. The nano-formulation with a PEG hydrophilic layer possesses a thick hydration layer, allowing it to remain stable in body fluids [41]. PEG has been extensively applied to enhance the property of nanoparticles. Accumulating evidence has suggested that PEGylation of nanoparticles prolongs their retention in blood circulation, increases their accumulation in tumor tissues, reduces their adherence to serum protein, and prevents their uptake by the reticuloendothelial system (RES) [42]. These nano-capsules exhibited a uniformly small size with enhanced stability, which could be delivered with high efficiency and prolong the retention time in circulation in vivo after administration. Previously, we have also demonstrated that BSA nanoparticles with an approximately neutral charge ( $\sim 0$  mV) can exhibit sufficient stability under physiological conditions in vivo with minimal particle aggregation in serum [34, 36, 43, 44].

In vitro cellular uptake experiments showed that the level of Anlotinib-nBSA- $^{131}\text{I}$  was much higher than that of free  $^{131}\text{I}$  in both 8305C and C643 ATC cell lines, and that interestingly, C643 cells with a higher EGFR expression level had a higher uptake efficiency than 8305C cells. The results suggested that anlotinib could induce endocytosis of Anlotinib-nBSA- $^{131}\text{I}$  and that uptake of Anlotinib-nBSA- $^{131}\text{I}$  was associated with the expression level of EGFR in the ATC cell lines.

EGFR is linked to the invasiveness and progression of TC [45], and is overexpressed in ATC. In ATC, EGF/EGFR could activate the PI3K/AKT and MAPK pathways, which are linked to aggressiveness and a poor prognosis [46]. In searching for the potential treatment targets in ATC, we first observed positive expressions of EGFR and mutant P53 in 80% and 60% of patients with ATC, respectively. Restoring *TP53* mutation may resensitize ATC cells to radiotherapy and meliorate clinical outcomes [18].

nBSA- $^{131}\text{I}$  displayed slightly stronger cytotoxicity than free  $^{131}\text{I}$  under the same radioactivity, which might be because of the enhanced permeability and retention (EPR) effect of the nano-capsule. Together with the findings that cytotoxicity was mostly similar between the Anlotinib-nBSA and free anlotinib groups at different concentrations, these data suggested the efficient

targeted delivery of  $^{131}\text{I}$  into ATC cells by Anlotinib-nBSA nanoparticles. The in vitro cytotoxicity assay findings further indicated that anlotinib and  $^{131}\text{I}$  in Anlotinib-nBSA- $^{131}\text{I}$  NPs exhibited an excellent enhanced effect. The NPs showed a more prominent dual therapeutic tumor-inhibition effect, which could be possibly explained by that anlotinib with an affinity towards VEGFR and EGFR on tumor cell surface was conjugated onto the surface of polymer NPs for precise targeting and antiangiogenic therapy, and that the Anlotinib-nBSA- $^{131}\text{I}$  NPs could transport  $^{131}\text{I}$  to tumor surface.

We found that  $^{131}\text{I}$ -Anlotinib-nBSA induced the strongest apoptotic effect in ATC cells.  $^{131}\text{I}$  is able to damage DNA and cause double-strand breaks (DSBs) by generating oxidizing free-radicals [33]. P53 responses to DSBs signals and induces cell apoptosis; thus, ATC cells harboring *TP53* mutation resist radiation. Our cell apoptosis assay revealed that anlotinib induced apoptosis of ATC cells, partly through upregulating P53 and activating the P53 pathway, which is consistent with previous reports [12, 47]. Therefore, it is possible that anlotinib weakens the radiotherapy resistance and increases the radiosensitivity of ATC cells by promoting the P53-induced apoptosis.

We found that apoptosis-related proteins were significantly upregulated by  $^{131}\text{I}$ -Anlotinib-nBSA, which is consistent with a previous report revealing that anlotinib upregulates the expression of P53 and Bax, and that anlotinib might induce apoptosis of TC cells through activating the P53 pathway [35]. Furthermore, when C643 cells were treated with Anlotinib-nBSA- $^{131}\text{I}$ , anlotinib improved the reaction sensitivity of  $^{131}\text{I}$  on activation of the P53-induced apoptosis pathway. It has been confirmed that anlotinib might be able to reactivate P53 mutants [35]. We hypothesize that three potential mechanisms may contribute to the antitumor effect of anlotinib in this study: First, anlotinib elevates the expression of P53, thus reactivating the P53 pathway which can upregulate the downstream elements including Bax; this induces cell apoptosis; second, anlotinib inhibits the EGFR downstream pathway PI3K-mTOR, and then decreases the expression of HIF-1 $\alpha$ ; third, mutant P53 elevates the sensitivity of VEGFR inhibitor [6, 11, 12].

In vivo SPECT/CT imaging showed an intense and persistent signal of tumor sites in all time during the one-week period of observation. The long-time tumor-specific distribution and retention of Anlotinib-nBSA suggested its potential use as a promising tumor-targeting nanocarrier. The in vivo biodistribution findings indicated that radioactive iodine obtained greater tumor homing ability and a long retention time in tumor site, by labeling on the Anlotinib-nBSA nanoparticles via an enhanced permeability and retention (EPR) effect. We hypothesize

that the drug would display double efficacy of anlotinib and  $^{131}\text{I}$ : Both the own antitumor effect of anlotinib with active targeting and the therapeutic efficacy of radionuclide with passively-transported  $^{131}\text{I}$  against tumor cells.

In vivo antitumor activity studies showed that Anlotinib-nBSA- $^{131}\text{I}$  treatment induced the greatest tumor growth delay, which could be possibly attributed to the radio-sensitization of anlotinib. The results indicated that  $^{131}\text{I}$  and anlotinib were successfully delivered to the tumor site through loading onto the nBSA nanoparticles and exerted a significant enhanced inhibitory effect against ATCs. In vivo biosafety evaluations further confirmed the safety of the innovative agent, Anlotinib-nBSA- $^{131}\text{I}$ .

## Conclusions

In this work, a precise targeted nanoparticles delivery system was innovatively constructed for the treatment and imaging of ATC. In vitro and in vivo studies both demonstrated that anlotinib sensitized ATC cells to  $^{131}\text{I}$  radionuclide therapy, via functional upregulation of P53. Furthermore, with the combined treatment effects of both anlotinib and  $^{131}\text{I}$  on nBSA, the nanoparticles were confirmed to have improved therapeutic efficacies. The efficient targeted nanocarriers were designed, which could be translated into improved therapeutic outcomes through the combination of  $^{131}\text{I}$  radiation and anlotinib's radio-sensibilization by upregulating P53 as well as its targeted cancer inhibition, providing a promising direction for enhanced targeted ATC therapy.

## Methods

### Materials

Anlotinib was developed by and bought from Chia-tai Tianqing Pharmaceutical Co., Ltd. in China.  $^{131}\text{I}$  radionuclide was provided by the HTA Co., Ltd. (China). RPMI-1640 medium, 88% DMEM medium, 10% fetal bovine serum (FBS), and Dead Cell Apoptosis Kit were purchased from Thermo Fisher Scientific Co. Ltd. (Shanghai, China). SA- $\beta$ -gal staining kit was purchased from Beyotime (Shanghai, China). Western blotting antibodies for P53 and Bax, and immunofluorescence antibodies for EGFR were purchased from Abcam. Western blotting antibodies for HIF-1 $\alpha$  were obtained from Santa-Cruz. Cell Counting Kit (CCK)-8 was purchased from Dojindo (Japan).

### Tissue sampling and immunohistochemical staining

ATC samples were collected from 15 patients admitted into four hospitals, including 2 from Xin Hua Hospital Affiliated to Shanghai Jiao Tong University School of Medicine, 2 from Shanghai Changhai Hospital, 8 from Peking Union Medical College Hospital, and 3 from First Affiliated Hospital of Harbin Medical University.

All patients were diagnosed with ATC via immunohistochemical analysis. Mutant P53 and EGFR proteins were immunohistochemically stained with anti-mutant P53 (cat. no.: PB0076, 1:1000) and anti-EGFR (cat. no.: H00001956-A01, 1:3000) monoclonal antibodies, respectively. Antibody-stained samples were observed under microscope at 400 $\times$  magnification. For mutant P53 staining, 100 cells in each of 10 random visual fields were evaluated per slide and samples were considered P53 positive when over 10% of the cancer cell nuclei showed strong staining (dark brown), as previously described[8]. For EGFR staining, evaluation was done based on the proportion of reactive cells within the cancers, and we searched for membranous staining in the samples and categorized the staining into 4 grades according to the proportion score which described the estimated fraction of positively stained cancer cells: 0 (no visible reaction), 1+ (<10% of the cancer cells were stained), 2+ (10–50% of the cancer cells were stained), and 3+ (50–100% of the cancer cells were stained). Grades 0 and 1+ were defined as negative, whereas Grades 2+ and 3+ which suggested >10% of cancer cells showed membranous staining of any intensity were defined as positive for EGFR, as previously described[48].

### Synthesis, characterization, and analysis of Anlotinib-nBSA nanoparticles

The positive-charge monomer N-(3-aminopropyl) methacrylamide (APM) was firstly enriched around the negatively-charged BSA, mainly through electrostatic interactions; while the other two reagents, the acid-degraded crosslinker, poly (ethylene glycol)-crosslinker (PEG-CL), and the neutral monomer, acrylamide (AAM), were enriched around the BSA molecules mainly through hydrogen bonding (Step 1). Subsequent polymerization was initiated by the addition of ammonium persulfate (APS) and tetramethylethylenediamine (TEMED) as the initiator, and the reaction solution was kept at 4  $^{\circ}\text{C}$  for 3 h (Step 2). The final BSA concentration was tuned to 1 mg/mL by diluting with phosphate buffer (50 mM, pH=7.0). Anlotinib was firstly modified with double-bond and then polymerized and attached onto nBSA through amidation with amino-groups on nBSA (Step 3). The polymer shells could effectively stabilize the interior BSA's tyrosine residue for further iodine labelling also with anlotinib. After the polymerization, the solution was dialyzed against PBS to remove by-products of small-molecules and all unreacted monomers. (Fig. 1).

The hydrodynamic diameter and zeta potential of Anlotinib-nBSA were detected using Zeta & Nano Sizer (Zetasizer Nano S, Malvern Instruments Ltd., Worcestershire, UK). Transmission electron microscope (TEM) samples were prepared by drop coating of 5  $\mu\text{L}$

nano-capsules onto carbon-coated copper grids. After 5 min, the excess samples were removed. The grid was then rinsed, and stained with 2% uranyl acetate. The morphologies of the NPs were observed using the TEM (Hitachi, Tokyo).

#### Radio-labelling nanoparticles by $^{131}\text{I}$ and examination of radioactive stability in vitro

Anlotinib-nBSA was radio-iodinated with  $^{131}\text{I}$  by the Iodogen method. 10  $\mu\text{l}$  [ $^{131}\text{I}$ ]NaI (700  $\mu\text{Ci}$ ) and 20  $\mu\text{l}$  nanoparticles (pH=7.4) were added into a tube with pre-coated Iodogen. The tube was incubated at 25  $^{\circ}\text{C}$  and shaken at 1000 revolutions per minute (rpm) for 10 min to accomplish the radioiodination. Then, the  $^{131}\text{I}$  nanoparticles were suspended in normal saline for further use. The radioiodine labeling rate was determined by TLC with ddH<sub>2</sub>O as the separation agent. To evaluate the stability of the radioiodine-labeled  $^{131}\text{I}$ -Anlotinib-nBSA in PBS (1 mM, pH=7.4) or serum at 37  $^{\circ}\text{C}$ , the radioiodine-labeling rates at 0, 3, 6, 12, and 24 h and 2 days were detected by TLC. The radioiodine-labeling rate (LR) was calculated using the following equation:

$$LR = \frac{P_t}{C_a} \times 100\%$$

where  $P_t$  and  $C_a$  were the sums of

counts measured for the target peaks and all chromatograms, respectively [20].

#### Cells and cell culture

8305C and C643 ATC cell lines were purchased from Zhong Qiao Xin Zhou Biotechnology Co., Ltd. (Shanghai, China). 8305C cells were cultured in 88% DMEM medium supplemented with 10% FBS, 1% Glutamax, and 1 mL NEAA (100 $\times$ ). C643 cells were cultured in RPMI-1640 medium supplemented with 10% FBS and 1% penicillin–streptomycin. Both kinds of cell lines grew in a humidified atmosphere containing 5% CO<sub>2</sub> at 37  $^{\circ}\text{C}$ .

#### Cell uptake assay

The cell uptake studies were carried out according to our previous report [20]. 8305C and C643 cells ( $5 \times 10^5$ ) were seeded into 24-well plates and incubated overnight. Then,  $^{131}\text{I}$ -Anlotinib-nBSA or free  $^{131}\text{I}$  were added into the medium (1  $\mu\text{Ci}$  per well). After 1 h, cells were rinsed using PBS for three times, and then NaOH-SDS (0.2 M NaOH, 1% sodium dodecyl sulfate, and SDS) was added. The cell lysates were collected and detected by a gamma-counter (SN-695, Solar Ring Photoelectric Instrument, Shanghai). In addition, a competitive inhibition group of the two cell lines was constructed, one hour before incubation with  $^{131}\text{I}$ -Anlotinib-nBSA.

#### In vitro cytotoxicity analysis

The cytotoxicity of NPs- $^{131}\text{I}$ , Anlotinib-nBSA, and Anlotinib-nBSA- $^{131}\text{I}$  was evaluated in C643 and 8305C cells by the CCK-8 assay. In brief,  $5 \times 10^3$  cells were seeded into 96-well plates and incubated overnight. Then, the culture medium was replaced with 100  $\mu\text{L}$  fresh medium, and different doses of NPs, NPs- $^{131}\text{I}$ , Anlotinib-nBSA, or Anlotinib-nBSA- $^{131}\text{I}$  were added. 48 h later, the culture medium was replaced and 10  $\mu\text{L}$  CCK-8 reagent was added into each well. After incubation for another 2 h, the absorbance value of each sample well was detected at 450 nm wavelength by a microplate reader (Varioskan Flash, Thermo Scientific). The wells with only cells seeded but without drugs were used as the control wells. Cells viability was determined as the absorbance ratio between the treatment and control wells.

#### Apoptosis-inducing effect and molecular mechanisms of anticancer effect

Firstly, C643 cells were planked into 6-well plates at a density of  $5 \times 10^5$  cells per well and then treated with different doses of normal saline, NPs- $^{131}\text{I}$  (300  $\mu\text{Ci}$  of  $^{131}\text{I}$ ), Anlotinib-nBSA (100  $\mu\text{g}$  of Anlotinib), or Anlotinib-nBSA- $^{131}\text{I}$  (300  $\mu\text{Ci}$  of  $^{131}\text{I}$ ) for 48 h. Then, saliniso-thiocyanate (FITC) and propidium iodide (PI) were added into the wells. After 15 min, all samples were analyzed by BD LSRFortessa flow cytometer. The C643 cells were pretreated under the same conditions as the apoptosis assay. In addition, proteins were extracted from the aforementioned groups, and the expressions of P53 (cat. no.: ab1101, Abcam), Bax (cat. no.: ab53154, Abcam), and HIF-1 $\alpha$  (cat. no.: 80R-1409, Fitzgerald) were evaluated by Western blot.

#### In vivo animal experiments

Male nude mice (4 weeks old) were used to develop the tumor models with subcutaneous C643 implant.  $5 \times 10^7$  C643 cells were suspended in 200  $\mu\text{L}$  medium (DMEM:matrigel (v/v)=1:1; Corning) and then injected subcutaneously into the nude mice. Tumor size was measured every other day to monitor tumor growth. All animals were maintained in a controlled environment with sufficient food and water. All the animal experiments were carried out strictly following the protocols approved by the Chinese Academy of Medical Sciences.

#### In vivo SPECT/CT imaging

SPECT/CT (MI Lab, The Netherlands) was used to characterize the in vivo imaging. All nude mice were blocked from thyroid by the gavage of cold NaI two days before imaging. To evaluate the in vivo behaviors of radioisotopes-labeled nBSA nanoparticles, nude mice loaded with C643 tumors were injected with free  $^{125}\text{I}$  or

$^{125}\text{I}$ -Anlotinib-nBSA (200  $\mu\text{Ci}/200\ \mu\text{L}$  of  $^{125}\text{I}$ ) intravenously via tail-vein, and then the radionuclide-imaging was acquired continuously by a small-animal SPECT/CT at various timepoints: 0.5 h, 3 h, 24 h, 2 days, and 5 days ( $n=5$  per group). During the entire image acquisition process, the nude mice were maintained under anesthesia by using 2.5% isoflurane. All SPECT/CT images were analyzed using the Pmod software (PMD Technologies LLC, USA).

### In vivo biodistribution

To quantitatively analyze the uptake of  $^{125}\text{I}$ -Anlotinib-nBSA in various organs and tissues, the nude mice were sacrificed at 24 h after intravenous injection. The tissues of tumor, heart, brain, lung, liver, spleen, kidney, muscle, and bone were collected and the radioactivity was measured by a gamma-counter (CRC-25R, Capintec. INC).

### Antitumor activity assay and biosafety evaluation

C643 tumor-bearing nude mice were randomly divided into 4 groups ( $n=5$ ). The mice were injected intravenously with saline, NPs- $^{131}\text{I}$  (300  $\mu\text{Ci}$  of  $^{131}\text{I}$ ), Anlotinib-nBSA (100  $\mu\text{g}$  of anlotinib), or Anlotinib-nBSA- $^{131}\text{I}$  (300  $\mu\text{Ci}$  of  $^{131}\text{I}$ ), respectively, when tumor volume reached about 100  $\text{mm}^3$ , and then received repeated injection every 3 days. Tumor size and nude mice weight were measured every other day. Tumor volumes were calculated as below: Tumor volume ( $\text{cm}^3$ ) = (length  $\times$  width $^2$ )/2. All nude mice were sacrificed at the 16th day after the first treatment. The tumor tissues were extracted, measured, weighed, and then immersed in 4% paraformaldehyde for hematoxylin and eosin (H&E) staining. The major organs, including heart, liver, lung, kidney, and spleen of each mouse were dissected for H&E staining.

### Statistical analysis

Data were presented as mean  $\pm$  standard error (SE) or stand deviation (SD) where appropriate. Student's *t*-test or analysis of variance (ANOVA) test was used to compare the differences between groups, and  $P < 0.05$  was considered to indicate statistical significance.

### Supplementary Information

The online version contains supplementary material available at <https://doi.org/10.1186/s12951-025-03223-2>.

Supplementary material 1.

### Acknowledgements

We would like to thank Liu Y and Lu YF for technical assistance and comments, and all the participants for their contributions to this study.

### Author contributions

Authors' Contributions Conception and design: Huang L, Zhang LL, and Cui Z Development of methodology: Zhang LL, Zhu C, Huang S, and Xu M Acquisition of data (acquired and managed patients, provided facilities, etc.) and performance of experiments: Zhang LL, Zhu C, Huang S, and Xu M Curation, analysis, and interpretation of data (e.g., statistical analysis, biostatistics, computational analysis): Huang L, Zhang LL, Li C, Fu H, Yin Y, and Cui Z Drafting of the manuscript: Huang L, Zhang LL, and Cui Z Writing, critical review, edition, and/or revision of the manuscript: Huang L and Zhang LL Administrative, technical, or material support (i.e., reporting or organizing data, constructing databases): Liang S, Cui Z, and Yin Y Study supervision: Huang L, Cui Z, Liang S, and Wang H.

### Funding

This research was supported by the National Natural Science Foundation of China (51703126) and the Scientific Research Start-up Fund for Excellent Doctor (Youbo; Class A; to Lei Huang) (The Third Batch) by The First Affiliated Hospital of Naval Medical University/Changhai Hospital, Naval Medical University. The funders played no role in study design; in the collection, analysis, or interpretation of data; in the writing of the report; or in the decision to submit the paper for publication.

### Availability of data and materials

Restrictions apply to the availability of the data for this study, which were used under license, and so are not publicly available.

### Declarations

#### Ethics approval and consent to participate

All samples were anonymously coded according to the local ethical guidelines as stipulated by the Declaration of Helsinki. Written informed consent was obtained from all the patients, and this study was approved by the Ethics Committee of Xinhua Hospital Affiliated to Shanghai Jiao Tong University School of Medicine and each participating center.

#### Consent for publication

Not applicable.

#### Competing interests

The authors declare no competing interests.

#### Author details

<sup>1</sup>Department of Nuclear Medicine, Xin Hua Hospital Affiliated to Shanghai Jiao Tong University School of Medicine, 1665 Kongjiang Road, Yangpu District, Shanghai 200092, China. <sup>2</sup>Department of Oncology, Xin Hua Hospital Affiliated to Shanghai Jiao Tong University School of Medicine, 1665 Kongjiang Road, Yangpu District, Shanghai 200092, China. <sup>3</sup>Shanghai Clinical Research and Trial Center, Shanghai 201210, China. <sup>4</sup>Department of Respiratory Medicine, Xin Hua Hospital Affiliated to Shanghai Jiao Tong University School of Medicine, Shanghai 200092, China. <sup>5</sup>Department of Gastroenterology, National Clinical Research Center for Digestive Diseases, The First Affiliated Hospital of Naval Medical University/Changhai Hospital, Naval Medical University, Shanghai 200433, China. <sup>6</sup>National Key Laboratory of Immunity and Inflammation, Changhai Clinical Research Unit, The First Affiliated Hospital of Naval Medical University/Changhai Hospital, Naval Medical University, 168 Changhai Road, Shanghai 200433, China.

Received: 4 April 2024 Accepted: 10 February 2025

Published online: 06 March 2025

### References

- Zhang L, Xu M, Zhang W, Zhu C, Cui Z, Fu H, Ma Y, Huang S, Cui J, Liang S, Huang L, Wang H. Three-dimensional genome landscape comprehensively reveals patterns of spatial gene regulation in papillary and anaplastic thyroid cancers: a study using representative cell lines for each cancer type. *Cell Mol Biol Lett*. 2023;28(1):1.
- Pugliese M, Fortunati N, Germano A, Asioli S, Marano F, Palestini N, Frairia R, Boccuzzi G, Catalano MG. Histone deacetylase inhibition affects

- sodium iodide symporter expression and induces 1311 cytotoxicity in anaplastic thyroid cancer cells. *Thyroid*. 2013;23(7):838–46.
3. Li Q, Zhang L, Lang J, Tan Z, Feng Q, Zhu F, Liu G, Ying Z, Yu X, Feng H, Yi H, Wen Q, Jin T, Cheng K, Zhao X, Ge M. Lipid-peptide-mRNA nanoparticles augment radioiodine uptake in anaplastic thyroid cancer. *Adv Sci*. 2023;10(3):e2204334.
  4. Jannin A, Escande A, Al Ghuzlan A, Blanchard P, Hartl D, Chevalier B, Deschamps F, Lamartina L, Lacroix L, Dupuy C, Baudin E. Anaplastic thyroid carcinoma: an update. *Cancers*. 2022;14(4):1061.
  5. Kim HS, Park YH, Lee J, Ahn JS, Kim J, Shim YM, Kim JH, Park K, Han J, Ahn MJ. Clinical impact of phosphorylated signal transducer and activator of transcription 3, epidermal growth factor receptor, p53, and vascular endothelial growth factor receptor 1 expression in resected adenocarcinoma of lung by using tissue microarray. *Cancer*. 2010;116(3):676–85.
  6. Fang S, Cheng W, Zhang M, Yang R. Association of TP53 mutations with response to anlotinib treatment in advanced non-small cell lung cancer. *Onco Targets Ther*. 2020;13:6645–50.
  7. Fallahi P, Ferrari SM, Galdiero MR, Varricchi G, Elia G, Ragusa F, Paparo SR, Benvenga S, Antonelli A. Molecular targets of tyrosine kinase inhibitors in thyroid cancer. *Semin Cancer Biol*. 2022;79:180–96.
  8. Liu L, Li D, Chen Z, Yang J, Ma Y, Cai H, Shan C, Lv Z, Zhang X. Wild-type P53 induces sodium/iodide symporter expression allowing radioiodide therapy in anaplastic thyroid cancer. *Cell Physiol Biochem*. 2017;43(3):905–14.
  9. Quiros RM, Ding HG, Gattuso P, Prinz RA, Xu X. Evidence that one subset of anaplastic thyroid carcinomas are derived from papillary carcinomas due to BRAF and p53 mutations. *Cancer*. 2005;103(11):2261–8.
  10. Yoo SK, Song YS, Lee EK, Hwang J, Kim HH, Jung G, Kim YA, Kim SJ, Cho SW, Won JK, Chung EJ, Shin JY, Lee KE, Kim JI, Park YJ, Seo JS. Integrative analysis of genomic and transcriptomic characteristics associated with progression of aggressive thyroid cancer. *Nat Commun*. 2019;10(1):2764.
  11. Shen G, Zheng F, Ren D, Du F, Dong Q, Wang Z, Zhao F, Ahmad R, Zhao J. Anlotinib: a novel multi-targeting tyrosine kinase inhibitor in clinical development. *J Hematol Oncol*. 2018;11(1):120.
  12. Ruan X, Shi X, Dong Q, Yu Y, Hou X, Song X, Wei X, Chen L, Gao M. Antitumor effects of anlotinib in thyroid cancer. *Endocr Relat Cancer*. 2019;26(1):153–64.
  13. Zhou AP, Bai Y, Song Y, Luo H, Ren XB, Wang X, Shi B, Fu C, Cheng Y, Liu J, Qin S, Li J, Li H, Bai X, Ye D, Wang J, Ma J. Anlotinib versus sunitinib as first-line treatment for metastatic renal cell carcinoma: a randomized phase II clinical trial. *Oncologist*. 2019;24(8):e702–8.
  14. Xu Q, Huang K, Meng X, Weng Y, Zhang L, Bu L, Zheng X, Cai J, Zhan R, Chen Q. Safety and efficacy of anlotinib hydrochloride plus temozolomide in patients with recurrent glioblastoma. *Clin Cancer Res*. 2023;29(19):3859–66.
  15. Elzoghby AO, Samy WM, Elgindy NA. Protein-based nanocarriers as promising drug and gene delivery systems. *J Control Release*. 2012;161(1):38–49.
  16. Guo L, Zhang H, Liu P, Mi T, Ha D, Su L, Huang L, Shi Y, Zhang J. Preclinical assessment of paclitaxel- and trastuzumab-delivering magnetic nanoparticles Fe<sub>3</sub>O<sub>4</sub> for treatment and imaging of HER2-positive breast cancer. *Front Med*. 2021;8: 738775.
  17. Wang Q, Sui G, Wu X, Teng D, Zhu L, Guan S, Ran H, Wang Z, Wang H. A sequential targeting nanoplatfor for anaplastic thyroid carcinoma theranostics. *Acta Biomater*. 2020;102:367–83.
  18. Huang S, Zhang L, Xu M, Li C, Fu H, Huang J, Jin X, Liang S, Wang H. Co-delivery of (131) I and prima-1 by self-assembled CD44-targeted nanoparticles for anaplastic thyroid carcinoma theranostics. *Adv Healthc Mater*. 2021;10(3): e2001029.
  19. Li J, Zhang L, Liu Y, Wen J, Wu D, Xu D, Segura T, Jin J, Lu Y, Wang H. An intracellular protein delivery platform based on glutathione-responsive protein nanocapsules. *Chem Commun*. 2016;52(93):13608–11.
  20. Wu J, Liang J, Liu R, Lv T, Fu K, Jiang L, Ma W, Pan Y, Tan Z, Liu Q, Qiu W, Ge M, Wang J. Autophagic blockade potentiates anlotinib-mediated ferroptosis in anaplastic thyroid cancer. *Endocr Relat Cancer*. 2023. <https://doi.org/10.1530/ERC-23-0036>.
  21. Liang J, Jin Z, Kuang J, Feng H, Zhao Q, Yang Z, Zhan L, Shen B, Yan J, Cai W, Cheng X, Qiu W. The role of anlotinib-mediated EGFR blockade in a positive feedback loop of CXCL11-EGF-EGFR signalling in anaplastic thyroid cancer angiogenesis. *Br J Cancer*. 2021;125(3):390–401.
  22. Wang C, Zhang R, Tan J, Meng Z, Zhang Y, Li N, Wang H, Chang J, Wang R. Effect of mesoporous silica nanoparticles co-loading with 17-AAG and Torin2 on anaplastic thyroid carcinoma by targeting VEGFR2. *Oncol Rep*. 2020;43(5):1491–502.
  23. Ferrari SM, Elia G, Ragusa F, Ruffilli I, La Motta C, Paparo SR, Patrizio A, Vita R, Benvenga S, Materazzi G, Fallahi P, Antonelli A. Novel treatments for anaplastic thyroid carcinoma. *Gland Surg*. 2020;9(Suppl 1):S28–s42.
  24. Gule MK, Chen Y, Sano D, Frederick MJ, Zhou G, Zhao M, Milas ZL, Galer CE, Henderson YC, Jasser SA, Schwartz DL, Bankson JA, Myers JN, Lai SY. Targeted therapy of VEGFR2 and EGFR significantly inhibits growth of anaplastic thyroid cancer in an orthotopic murine model. *Clin Cancer Res*. 2011;17(8):2281–91.
  25. Gomez-Rivera F, Santillan-Gomez AA, Younes MN, Kim S, Fooshee D, Zhao M, Jasser SA, Myers JN. The tyrosine kinase inhibitor, AZD2171, inhibits vascular endothelial growth factor receptor signaling and growth of anaplastic thyroid cancer in an orthotopic nude mouse model. *Clin Cancer Res*. 2007;13(15 Pt 1):4519–27.
  26. Zheng X, Wang J, Ye T, Tang W, Pan X, Wang S, Liu J. Efficacy and safety of anlotinib-based chemotherapy for locally advanced or metastatic anaplastic thyroid carcinoma. *Endocrine*. 2023;81(3):540–6.
  27. Ejjah V, Owoseni O, Bataille-Backer P, Ogundiye OD, Fisusi FA, Adesina SK. Approaches to improve macromolecule and nanoparticle accumulation in the tumor microenvironment by the enhanced permeability and retention effect. *Polymers*. 2022;14(13):2601.
  28. Shinde VR, Revi N, Murugappan S, Singh SP, Rengan AK. Enhanced permeability and retention effect: a key facilitator for solid tumor targeting by nanoparticles. *Photodiagn Photodyn Ther*. 2022;39: 102915.
  29. Yang C, Tan Y, Qi H, Zhou J, Long L, Zhan Q, Wang Y, Yuan X, Kang C. Boosting of the enhanced permeability and retention effect with nanocapsules improves the therapeutic effects of cetuximab. *Cancer Biol Med*. 2020;17(2):433–43.
  30. Zou X, Jiang Z, Li L, Huang Z. Selenium nanoparticles coated with pH responsive silk fibroin complex for fngolimod release and enhanced targeting in thyroid cancer. *Artificial Cells Nanomed Biotechnol*. 2021;49(1):83–95.
  31. Shi Y, van der Meel R, Chen X, Lammers T. The EPR effect and beyond: strategies to improve tumor targeting and cancer nanomedicine treatment efficacy. *Theranostics*. 2020;10(17):7921–4.
  32. Kang H, Rho S, Stiles WR, Hu S, Baek Y, Hwang DW, Kashiwagi S, Kim MS, Choi HS. Size-dependent EPR effect of polymeric nanoparticles on tumor targeting. *Adv Healthcare Mater*. 2020;9(1): e1901223.
  33. Schumann S, Scherthan H, Pfestroff K, Schoof S, Pfestroff A, Hartrampf P, Hasenauer N, Buck AK, Luster M, Port M, Lassmann M, Eberlein U. DNA damage and repair in peripheral blood mononuclear cells after internal ex vivo irradiation of patient blood with (131)I. *Eur J Nucl Med Mol Imaging*. 2022;49(5):1447–55.
  34. Liang S, Jin X, Ma Y, Guo J, Wang H. Folic acid-conjugated BSA nanocapsule (n-BSA-FA) for cancer targeted radiotherapy and imaging. *RSC Adv*. 2015;5(108):88560–6.
  35. Han Y, Wang J, Sun T, Ouyang Q, Li J, Yuan J, Xu B. Predictive biomarkers of response and survival following immunotherapy with a PD-L1 inhibitor benmelstobart (TQB2450) and antiangiogenic therapy with a VEGFR inhibitor anlotinib for pretreated advanced triple negative breast cancer. *Signal Transduct Target Ther*. 2023;8(1):429.
  36. Liu Y, Du J, Yan M, Lau MY, Hu J, Han H, Yang OO, Liang S, Wei W, Wang H, Li J, Zhu X, Shi L, Chen W, Ji C, Lu Y. Biomimetic enzyme nanocomplexes and their use as antidotes and preventive measures for alcohol intoxication. *Nat Nanotechnol*. 2013;8(3):187–92.
  37. Prasad R, Aiyer S, Chauhan DS, Srivastava R, Selvaraj K. Bioresponsive carbon nano-gated multifunctional mesoporous silica for cancer theranostics. *Nanoscale*. 2016;8(8):4537–46.
  38. Chauhan DS, Kumawat MK, Prasad R, Reddy PK, Dhanka M, Mishra SK, Bahadur R, Neekhra S, De A, Srivastava R. Plasmonic carbon nanohybrids for repetitive and highly localized photothermal cancer therapy, colloids and surfaces. *B, Biointerfaces*. 2018;172:430–9.
  39. Prasad R, Jain NK, Yadav AS, Jadhav M, Radharani NNV, Gorain M, Kundu GC, Conde J, Srivastava R. Ultrahigh penetration and retention of graphene quantum dot mesoporous silica nanohybrids for image guided tumor regression. *ACS Appl Bio Mater*. 2021;4(2):1693–703.
  40. Bindra AK, Sreejith S, Prasad R, Gorain M, Thomas R, Jana D, Nai MH, Wang D, Tharayil A, Kundu GC, Srivastava R, Thomas S, Lim CT, Zhao Y.

A plasmonic supramolecular nanohybrid as a contrast agent for site-selective computed tomography imaging of tumor. *Adv Funct Mater.* 2022;32(12):2110575.

41. Li R, Yan J, Xie L, Zhang Y, Gao J, Liu Q, Lin Z, Jiang P, Qian H, Yang M, Wu F, Jiang X, Liu B, Wang L. Facile optimization and evaluation of PEG-PCL block copolymeric nanoparticles for anticancer drug delivery using copolymer hybrids and histoculture drug response assays. *J Biomed Nanotechnol.* 2018;14(2):321–30.
42. Sun CY, Shen S, Xu CF, Li HJ, Liu Y, Cao ZT, Yang XZ, Xia JX, Wang J. Tumor acidity-sensitive polymeric vector for active targeted siRNA delivery. *J Am Chem Soc.* 2015;137(48):15217–24.
43. Zhang L, Liu Y, Liu G, Xu D, Liang S, Zhu X, Lu Y, Wang H. Prolonging the plasma circulation of proteins by nano-encapsulation with phosphorylcholine-based polymer. *Nano Res.* 2016;9(8):2424–32.
44. Liang S, Liu Y, Jin X, Liu G, Wen J, Zhang L, Li J, Yuan X, Chen ISY, Chen W, Wang H, Shi L, Zhu X, Lu Y. Phosphorylcholine polymer nanocapsules prolong the circulation time and reduce the immunogenicity of therapeutic proteins. *Nano Res.* 2016;9(4):1022–31.
45. Janković J, Tatić S, Božić V, Živaljević V, Cvejić D, Paskaš S. Inverse expression of caveolin-1 and EGFR in thyroid cancer patients. *Hum Pathol.* 2017;61:164–72.
46. Milosevic Z, Pesic M, Stankovic T, Dinic J, Milovanovic Z, Stojisic J, Dzodic R, Tanic N, Bankovic J. Targeting RAS-MAPK-ERK and PI3K-AKT-mTOR signal transduction pathways to chemosensitize anaplastic thyroid carcinoma. *Transl Res.* 2014;164(5):411–23.
47. Lorusso L, Pieruzzi L, Biagini A, Sabini E, Valerio L, Giani C, Passannanti P, Pontillo-Contillo B, Battaglia V, Mazzeo S, Molinaro E, Elisei R. Lenvatinib and other tyrosine kinase inhibitors for the treatment of radioiodine refractory, advanced, and progressive thyroid cancer. *Onco Targets Ther.* 2016;9:6467–77.
48. Lee DH, Lee GK, Kong SY, Kook MC, Yang SK, Park SY, Park SH, Keam B, Park DJ, Cho BY, Kim SW, Chung KW, Lee ES, Kim SW. Epidermal growth factor receptor status in anaplastic thyroid carcinoma. *J Clin Pathol.* 2007;60(8):881–4.

## Publisher's Note

Springer Nature remains neutral with regard to jurisdictional claims in published maps and institutional affiliations.